A Non-Resonant Multi-Output Half-Bridge Inverter for Flexible Cooking Surfaces

Felix Rehm*, Marc Hiller
Elektrotechnisches Institut (ETI), Karlsruhe Institute of Technology (KIT), Karlsruhe, Germany
*E-mail: felix.rehm@kit.edu

***Abstract*—In domestic induction heating (IH) appliances most commonly the series resonant half-bridge (HB) inverter is used. The number of required components can be further reduced by using non-resonant inverter topologies. Within this contribution, a novel non-resonant multi-output HB inverter for use in flexible cooking surfaces is presented. The proposed inverter topology is described and simulation as well as measurement results are shown. Measurement results are presented for operation with up to two inductors. The hardware prototype is equipped with gallium nitride semiconductors and operates at switching frequencies up to 400 kHz. Measurement results show that an output power of 522 W is reached for use of a single inductor. When using two inductors, a maximum output power of 828 W is reached. The presented results demonstrate the feasibility of the concept, while the efficiency of the system needs to be investigated in future work.**

***Index Terms*—domestic induction heating, gallium nitride, multicoil system, wireless power transfer**

I. Introduction

In contrast to electric-resistive stoves or gas burners, when using induction heating (IH) the heat is generated directly within the cookware. For this, an alternating current in the frequency range above $20\,\mathrm{kHz}$ is forced to flow through an inductor. The inductor is made from spiral wound copper wire - typically litz wire - and ferromagnetic material, which acts as flux concentrator. The current through the inductor generates an alternating magnetic field of the same frequency. Due to Faraday's law, a current is flowing through the electrical conductive bottom layer of the cookware. As a result, ohmic losses are generated within the cookware and electrical energy is converted into thermal energy. Additionally, if the cookware bottom layer is made out of ferromagnetic material, hysteresis losses are generated as well [1], [2].

For domestic IH systems, mainly two different types of cooktops are distinguished. Conventional IH systems make use of a dedicated number of inductors with an outer diameter d_o in the range of approximately $140\,\mathrm{mm}$ to $280\,\mathrm{mm}$. The inductors are designed, such that the use of a single pot above a dedicated inductor is possible. The maximum amount of pots, which can be used in parallel, is restricted to the number of inductors within the system and the diameter of the inductors is dependent on the diameter of the cookware to be used. To increase the flexibility, two concentric wound windings can be used to form an adaptable-diameter inductor in order to increase the range of suitable pot diameters [3]. Additionally, a better use of the power electronics is possible, if the inductor diameter is adapted to the pot diameter. However, the maximum amount of pots to be used is limited.

To overcome this limitation, several different approaches are used for flexible cooking surfaces. Inductors with an outer diameter of $d_\mathrm{o} = 180\,\mathrm{mm}$ are overlapped in [4] to build a flexible cooking zone. Herein, each inductor is rated with a nominal power of up to $2.8\,\mathrm{kW}$. The approach described in [5] makes use of multiple non-overlapping inductors of small diameter with a nominal power of $600\,\mathrm{W}$ each. A system design consisting of multiple small inductors allows the user to place multiple pots anywhere on the cooktop. Therefore, flexible cooking surfaces increase the user experience as they offer more flexibility in use [6].

To supply the inductors with an AC voltage, several inverter topologies are used. The most commonly used inverter topology in conventional IH systems is the series resonant half-bridge (HB) inverter [7]. As shown in Fig. 1, it consists of an high-side and a low-side switch. Most commonly, IGBTs are used as swichting devices, while MOSFETs can be used too [8]. The inductor, which describes the IH load, is modeled as a series connection of the equivalent inductance L_eq and the equivalent resistance R_eq. A resonant capacitor C_res is connected in series to complete the resonant tank. To better accomplish to electromagnetic compatibility (EMC) standards and improve high frequency behavior of the inverter, the resonant capacitor is typically split into two capacitors of value $C_\mathrm{res}/2$.

In flexible cooking surfaces, several different inverter topologies are used [9]. The approach presented in [10] makes use of multiple resonant HB inverters connected in parallel to a common DC bus. For each inverter, two semiconductor switches and two resonant capacitors are needed. To reduce the number of required semiconductor switches, a multiple-output resonant zero-voltage switching (ZVS) inverter is presented in [5]. The matrix arrangement of the inverter branches allows

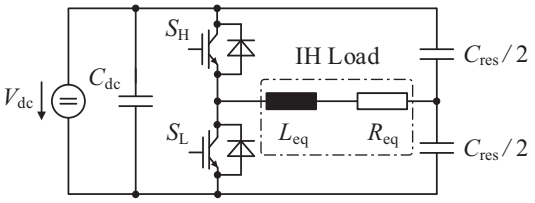

Fig. 1. Equivalent circuit diagram of series resonant half-bridge inverter.

to reduce the number of semiconductor switches to 2·ceil($\sqrt{n}$), with n being the number of inductors. The amount of diodes in this topology is given by $2\cdot(n+\cdot\text{ceil}(\sqrt{n}))$. By using zero-current switching (ZCS), the topology presented in [11] allows to reduce the number of required diodes to $2 \cdot n$.

Due to reduced switching losses compared to silicon based semiconductor devices, wide bandgap (WBG) semiconductor devices are dedicated for use within IH systems [10], [12]. The use of WBG devices offers the opportunity to use non-resonant inverter topologies as presented in [13]. Herein, a non-resonant full-bridge (FB) inverter for use in a conventional IH system is described. A main drawback of a FB inverter is the use of four semiconductor devices, instead of two, which are needed in a HB inverter. Applied to a flexible cooking surface, the number of required semiconductor devices would result in $4 \cdot n$.

Nevertheless, in this contribution it is shown that a non-resonant multi-output HB inverter can be used for flexible cooking surfaces. Due to the non-resonant topology no resonant capacitors are needed and the number of semiconductor devices needed is given by $2 \cdot n$.

In the remainder of this paper, the proposed inverter topology is introduced, a method for characterization of load parameters is presented and the modulation scheme to control the output power of the inverter is described. To demonstrate the feasibility of the proposed inverter topology, measurement results from a hardware prototype are shown.

II. Proposed Architecture

A. Inverter Topology

The proposed inverter topology consists of multiple HBs connected in parallel to a common DC bus. An inductor with an outer diameter of 70 mm is connected to each output of the inverter. The equivalent circuit diagram of the proposed inverter topology is shown in Fig. 2. One terminal of each inductor is connected to the output of a HB, while the other end is connected to node N_0. Within this contribution a hardware prototype consisting of 13 parallel HBs is discussed. A schematic of the hardware setup with the printed circuit board (PCB), the inductors, the ceramic glass and a pot is shown in Fig. 3.

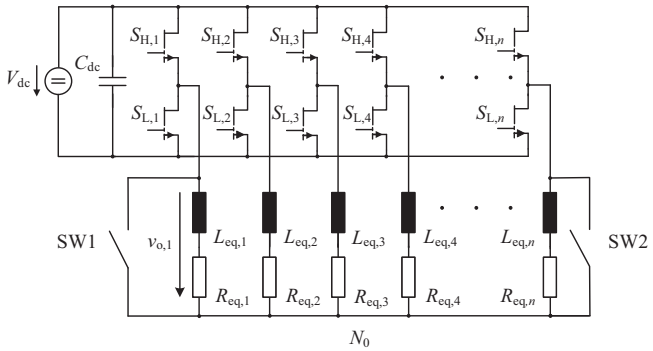

Fig. 2. Equivalent circuit diagram of proposed inverter topology with L_{eq} and R_{eq} ($i \in [1, n]$) representing the equivalent impedance of the inductors.

During operation, it has to be ensured that a single inductor can be used. Therefore, additional switches (see SW1 and SW2 in Fig. 2) are needed to provide a current return path. Operation of the inverter can then be performed in HB and FB configuration. Assuming a duty cycle $D = 0.5$ for each semiconductor of one HB, the maximum rms-value of the first harmonic of the output voltage $V^1_{o,i}$ is given by

$$V^1_{o,i} = \frac{\sqrt{2}}{\pi} \cdot V_{dc} \tag{1}$$

with V_{dc} as common DC-Link voltage. For FB operation, this value is doubled, such that the maximum rms-value of the first harmonic leads to

$$V^1_{o,i} = \frac{2\sqrt{2}}{\pi} \cdot V_{dc}. \tag{2}$$

A detailed description of modulation and power control of the inverter is given in Section II-C.

B. Characterization of Load Parameters

Modeling of the electromagnetic part of an IH system can be performed using different models. Within this contribution, the model introduced in [14] is used. Herein, the equivalent impedance model is described as a series connection of an equivalent inductance L_{eq} and an equivalent resistor R_{eq} and represents the electromagnetic behaviour of the coupled inductor-pot system. In general, not only the power transferred to the cookware is represented by R_{eq}, but also loss effects within the coil, such as copper losses, losses within the flux concentrators and the aluminum shielding. For the sake of simplicity, in the following loss effects generated within the inductors are neglected. This means that the presented simulation results for R_{eq}, only represent the power transferred to the pot caused by eddy-current losses within the ferromagnetic bottom of the pot.

As described in [14], the parameter values of L_{eq} and R_{eq} are dependent on the operating point of the inductor given through the inductor current i_L and its frequency f. To determine the values of the equivalent impedance, two-dimensional Finite-Element-Analyses (FEA) are performed for a single inductor beneath a pot. The inductors with an outer diameter $d_o = 70\,\text{mm}$ are made out of a ferrite pot core (see

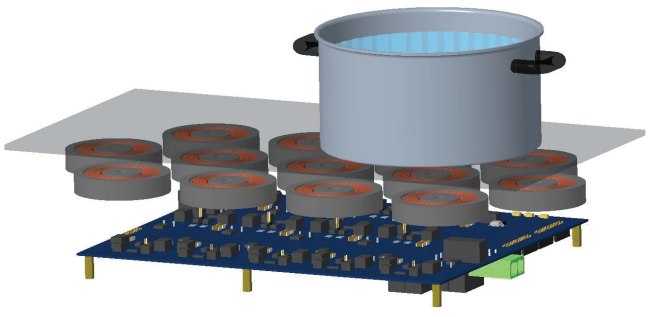

Fig. 3. Schematic of hardware setup of a flexible cooking surface with PCB, inductors and pot shown.

Fig. 3). The initial relative permeability μ_i of the ferrites is given by $\mu_\mathrm{i} = 2400$. A coil made from litz wire with 11 turns is placed within the ferrite core. The litz wire has $n_\mathrm{s} = 600$ strands with a diameter of $d_\mathrm{s} = 71\,\mu\mathrm{m}$ of a single strand. The material parameters of the ferromagnetic bottom of the pot are taken from [15].

The values of L_eq and R_eq for a single inductor beneath a pot in dependence of the effective current through the inductor I_L and its frequency f is shown in Fig. 4 and Fig. 5. In Fig. 4 it can be seen, that the equivalent inductance L_eq is decreasing with increasing values of inductor current I_L and frequency f. This behaviour can be explained with saturation of the magnetic material within the pot bottom for higher values of I_L. With increasing frequency, the current density within the pot bottom is increasing. The current in the pot bottom is generating a magnetic field which is opposing the magnetic field of the inductor. As a result the equivalent inductance L_eq is decreasing with frequency f. Contrarily, the value of R_eq is increasing with f as the losses generated within the pot are also increasing with frequency. Due to magnetic saturation of the pot bottom, the values of R_eq are decreasing for higher values of inductor current I_L.

C. Modulation and Power Control

The proposed inverter topology can be used in different operating modes, which are distinguished by a different modulation and power control scheme. The operating mode to be used depends on the number of active inductors. In the following, the three different operating modes shown in Fig. 6 are analyzed. All further operating modes can be derived from these three modes.

A possible operating mode of a flexible cooking surface is, that a single pot with small size is placed on the cooktop. Therefore, it has to be ensured, that a single inductor can be driven. To achieve this, a single inductor can be operated in FB operating mode of the inverter when SW1 or SW2 (see Fig. 6(a)) is closed.

The output power of the inverter can be calculated by

$$P_\mathrm{o} = \sum_{i=1}^{13} \frac{1}{T} \int_0^T p(t)\,\mathrm{d}t = \sum_{i=1}^{13} \frac{1}{T} \int_0^T v_{\mathrm{o},i} \cdot i_{\mathrm{o},i}\,\mathrm{d}t, \quad (3)$$

with $v_{\mathrm{o},i}$ being the voltage over and $i_{\mathrm{o},i}$ being the current through an inductor (exemplary shown for inductor 1 in Fig. 6(a)). T describes the period time and is defined as $T = 1/f$. In Fig. 7(a) simulation results for the output power of the inverter are shown over frequency f for the operating modes shown in Fig. 6 at a DC-Link voltage of $V_\mathrm{dc} = 325\,\mathrm{V}$. Due to the ohmic-inductive characteristic of the inverter load, the output power decreases with increasing frequency. Since a single inductor can only be operated in FB operating mode, the applied voltage over a single inductor is doubled compared to operation in HB mode (see eq. (1) and eq. (2)). Hence, the output current I_o is higher when using a single inductor compared with the use of multiple inductors, as can be seen in Fig. 7(b). Furthermore, the output power is not linearly decreasing over frequency f. For the use of a single inductor at $500\,\mathrm{kHz}$, a power of approximately $450\,\mathrm{W}$ is transferred to the cookware. To further decrease the transferred power, much higher frequencies than $500\,\mathrm{kHz}$ are needed.

To gain another degree of freedom in controlling the output power, a control strategy is used, that employs square-wave control with variable switching frequency in combination with phase-shift modulation. In the following, this type of control is referred to as VFPS. In conventional IH systems, power control is achieved using a variable switching frequency and a variable duty cycle (VFDC) [16]. In contrast to VFDC, the duty cycle remains constant at $D = 0.5$ at VFPS. Due to the possibility to operate the inverter in FB mode, the switching times of the high-side transistors can be varied relatively to each other. Exemplary waveforms of the gate signals and the resulting output voltage $v_{\mathrm{o},1}$ are given in Fig. 8 for the operating mode shown in Fig. 6(a). The variable to be

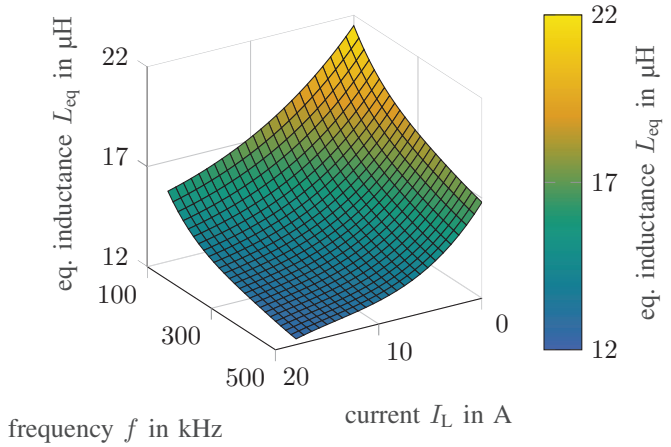

Fig. 4. Equivalent inductance L_eq of a single inductor beneath a pot in dependence of rms-value of inductor current I_L and its frequency f.

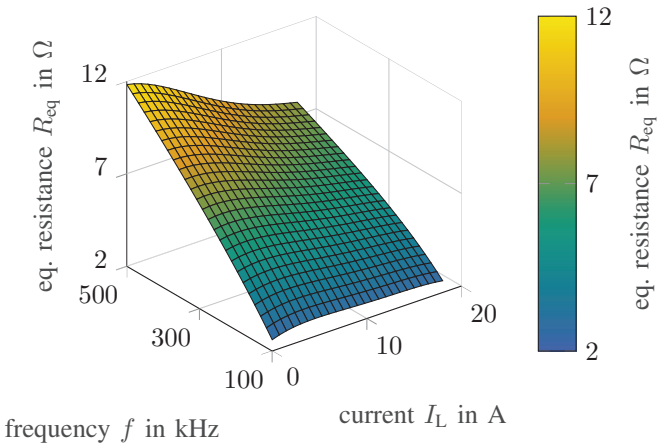

Fig. 5. Equivalent resistance R_eq of a single inductor beneath a pot in dependence of rms-value of inductor current I_L and its frequency f.

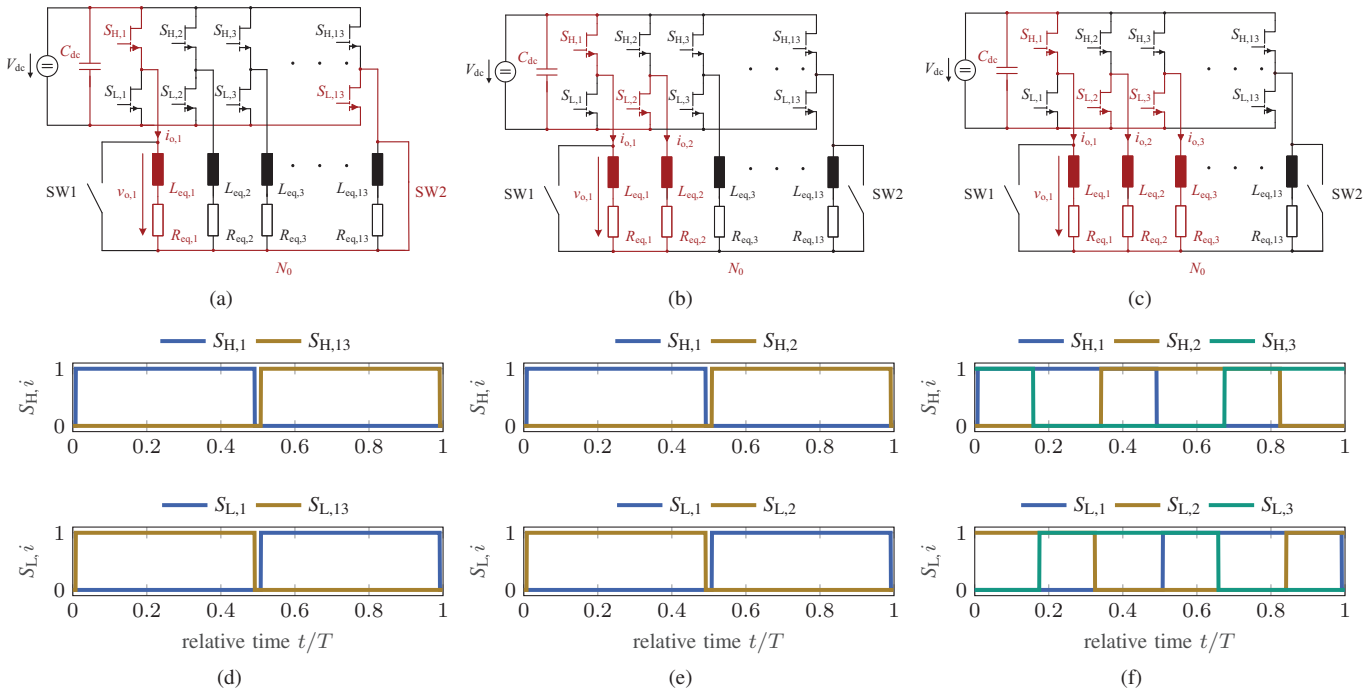

Fig. 6. Three exemplary operating modes of the proposed inverter with (a) use of single inductor in FB operating mode, (b) use of two inductors and (c) use of three inductors. Corresponding gate signals for a duty cycle $D = 0.5$ and phase shift angle $\beta = 180°$ are shown for one period with $T = 1/f$ in subfigures (d)-(f). Operating modes with another amount of inductors used can be derived based on the operating modes shown.

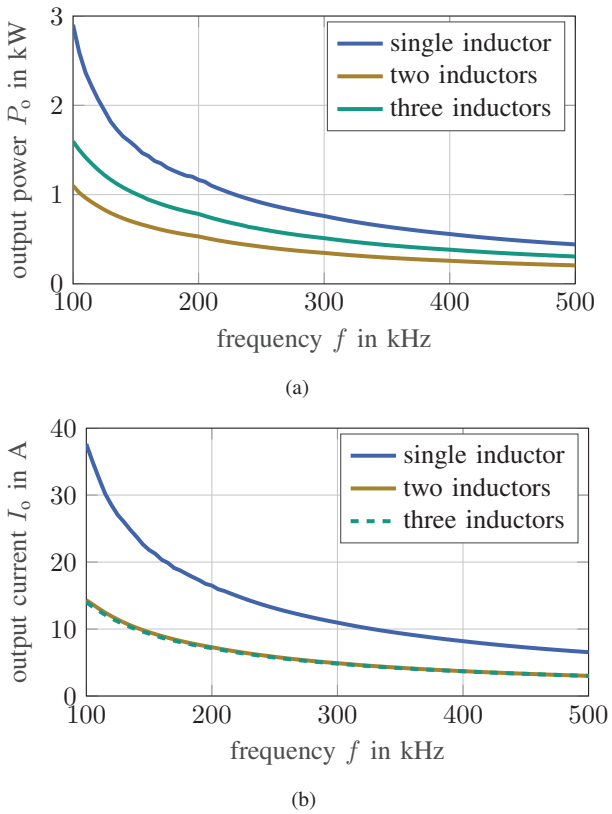

Fig. 7. Simulation results of (a) output power P_o and (b) rms-value of output current I_o of the inverter over frequency f for a single inductor as well as for two and three inductors for DC-Link voltage $V_{dc} = 325\,\mathrm{V}$ and fixed duty cycle $D = 0.5$.

controlled is the phase-shift angle β which is defined as

$$\beta = \beta_2 - \beta_1 \tag{4}$$

with β_1 and β_2 as the electrical angles at which transistors $S_{H,1}$ and $S_{H,13}$ are turned on. The rms-value of the first harmonic of the output voltage $V^1_{o,1}$ is given by

$$V^1_{o,1} = \frac{2 \cdot \sqrt{2}}{\pi} \cdot V_{dc} \cdot \sin\left(\frac{\beta}{2}\right). \tag{5}$$

Therefore, the output power of the inverter can be controlled independently of the value of V_{dc}. This fact is depicted in Fig. 9, which shows simulation results of the output power over phase-shift angle β for different values of the DC-Link voltage V_{dc} at frequency $f = 200\,\mathrm{kHz}$.

III. Hardware Prototype and Measurement Results

A. Specifications

To show the feasibility of the proposed concept and validate the simulation results a hardware prototype is built. The hardware components and specifications of the prototype are given in Table I. The hardware prototype is equipped with 13 half-bridges, which are connected to a common DC bus. The semiconductor devices are gallium nitride (GaN) high-electronmobility transitors (HEMT) of manufacturer *GaN Systems*. The two GaN-HEMTs of each HB are connected with the thermal interface material (TIM) *GEL 130 S 05* from *Fischer Elektronik* to the active heatsink *HF19-22* from *European Thermodynamics* with dimensions of 18.5 mm x 18.8 mm x 22 mm.

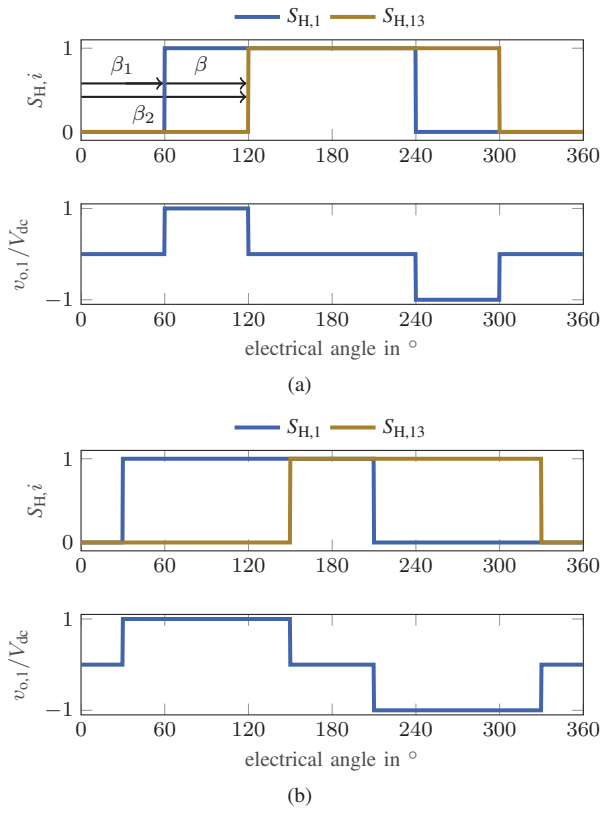

Fig. 8. Exemplary waveforms of high-side gate signals as well as resulting relative output voltage $v_{o,1}/V_{dc}$ for use of phase-shift control with (a) phase-shift angle $\beta = 60°$ and (b) phase-shift angle $\beta = 120°$.

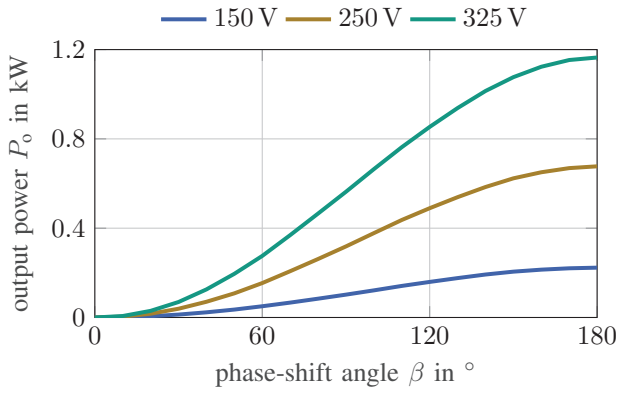

Fig. 9. Simulation results of output power P_o over phase-shift angle β for different values of DC-Link voltage V_{dc} for operation of inverter with a single inductor at frequency $f = 200\,\text{kHz}$.

TABLE I
HARDWARE COMPONENTS AND SPECIFICATIONS OF PROTOTYPE

Component / Parameter	Symbol	Value	
Semiconductor switches	$S_{H/L,i}$	GaN Systems *GS66506T*	
No. of inductors	N	13	
Max. DC-Link voltage	V_{dc}	400	V
Max. switch. frequency	f	500	kHz
Max. output current	$I_{o,i}$	10	A
DC-Link capacitance	C_{dc}	22.4	µF

B. Modulation Scheme

To demonstrate the current and voltage waveforms, two exemplary operating points are discussed in this section. For the hardware prototype described in Sec. III-A, measuring of the output voltages is performed using high voltage differential probes of type *PMK BumbleBee*, current sensing is performed using *Keysight N2783b* current probes. The oscilloscope used is *HRO 64Zi* from *LeCroy* with four channels, 12-bit resolution and a bandwidth of 400 MHz.

Voltage and current waveform graphs for two operating points are shown in Fig. 10. Fig. 10(a) shows the output voltage $v_{o,1}$ and the current through the inductor $i_{o,1}$ for operation of a single inductor in FB mode as given in Fig. 6(a) at a DC-Link voltage V_{dc} of 325 V and a frequency f of 200 kHz. In Fig. 10(b), measurement results for operation of two inductors (see Fig. 6(b)) are shown. The voltage depicted is the output voltage of the inverter, which is $v_{o,1} - v_{o,2}$. In this operating point, the DC-Link voltage V_{dc} is 325 V and the frequency f is 140 kHz. Using the measured values of output voltage and output current, the output power of the inverter can be calculated according to eq. (3). Comparison of Fig. 10(a) and Fig. 10(b) shows that the amplitude of the inductor current $i_{o,1}$ is approximately the same in both operating points. Even though the number of inductors is doubled, the output power is not doubled due to the fact that the frequency is not the same in both operating points.

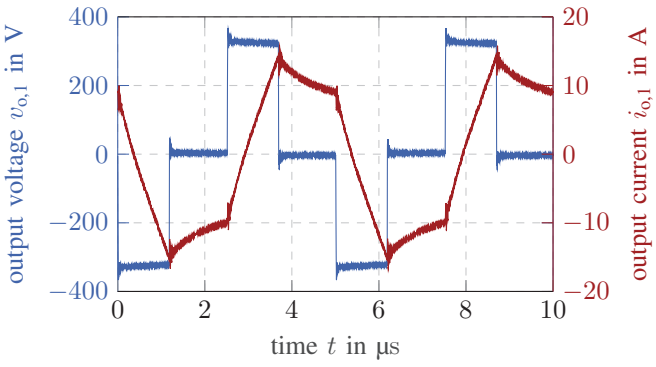

(a) $f = 200\,\text{kHz}$, $\beta = 85°$, $P_o = 522\,\text{W}$

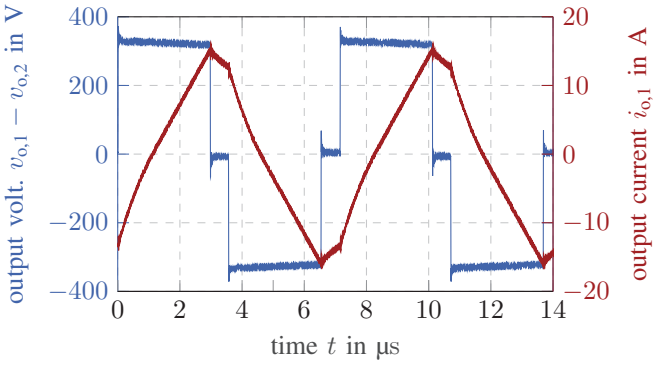

(b) $f = 140\,\text{kHz}$, $\beta = 150°$, $P_o = 754\,\text{W}$

Fig. 10. Measurement results for operation with (a) single inductor and (b) two inductors at $V_{dc} = 325\,\text{V}$

C. Power Control

The simulation results shown in Sec. II-C are validated for the proposed power control schemes. Therefore, measurements are performed for operating modes shown in Fig. 6(a) and (b) for varying frequency f and varying phase-shift angle β. Due to the fact that the output current is less than 10 A only for frequencies higher than 320 kHz when using a single inductor (see blue curve Fig. 7(b)), power control with a variable phase-shift angle β is necessary.

Measurement results for power control with a variable phase-shift angle are shown in Fig. 11 for different values of V_{dc}. As to be seen, the simulation results can be validated and a maximum output power of 522 W is reached at frequency $f = 200\,\mathrm{kHz}$ at $V_{\mathrm{dc}} = 325\,\mathrm{V}$ with a phase-shift angle $\beta = 85°$. Power control with varying frequency f and a fixed phase-shift angle $\beta = 180°$ is shown in Fig. 12. To not exceed the maximum output current, measurements are performed only for $V_{\mathrm{dc}} = 150\,\mathrm{V}$.

Besides the measurements with one inductor, measurements were also performed with a series connection of two inductors as shown in Fig. 6(b). For a DC-Link voltage of $V_{\mathrm{dc}} = 325\,\mathrm{V}$, the output power of the inverter is controlled through varying phase-shift angle β (Fig. 13) and varying frequency f (Fig. 14). Contrarily to the results presented for operation with a single inductor, there is a higher deviation between measurement and simulation results for the use of two inductors. A possible explanation for this, is the modeling of the inductors. As described in Sec. II-B, parameter values of the inverter load are determined through FEA simulation of a single inductor. However, the magnetic behavior of the two inductors is not independent from each other [17], which is not observed in the FEA simulations. Nevertheless, Fig. 13 shows that at a phase-shift angle $\beta = 180°$ a maximum output power of 828 W is reached.

IV. Conclusion and Outlook

In this contribution, a non-resonant inverter topology for use in a flexible cooking surface is presented. In contrast to resonant inverter topologies, no resonant capacitors are required. Compared to inverters with a matrix structure the number of required semiconductor switches is higher. However, the semiconductor switches can be rated according to the maximum power of a single load. This fact offers advantages in terms of a simple modularization as well as scalability.

To demonstrate the feasibility of the non-resonant inverter concept, a hardware prototype, equipped with GaN-HEMTs,

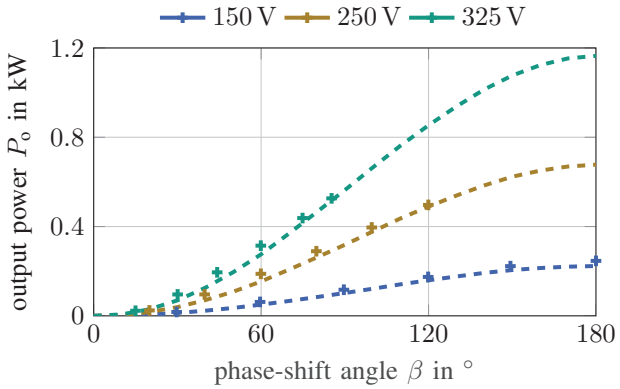

Fig. 11. Measurement (+) and simulation results (- -) of output power P_o for operation of a single inductor at varying DC-Link voltage and varying phase-shift angle β at frequency $f = 200\,\mathrm{kHz}$.

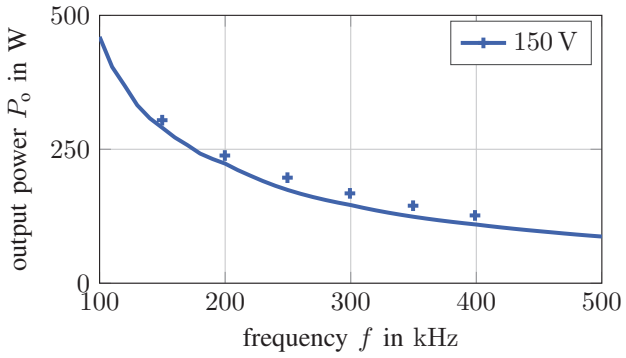

Fig. 12. Measurement (+) and simulation results (–) of output power P_o for operation of a single inductor at DC-Link voltage $V_{\mathrm{dc}} = 150\,\mathrm{V}$ and varying frequency f at constant phase-shift angle $\beta = 180°$.

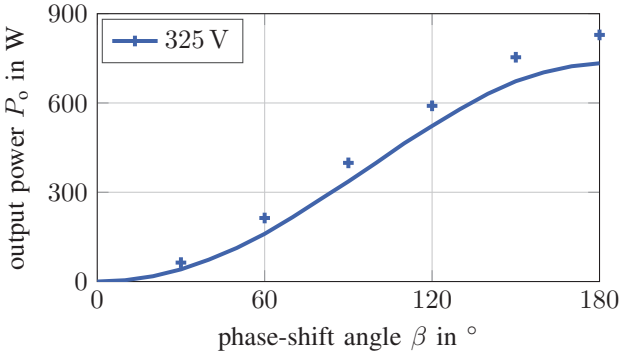

Fig. 13. Measurement (+) and simulation results (–) of output power P_o for operation of two inductors at DC-Link voltage $V_{\mathrm{dc}} = 325\,\mathrm{V}$ and varying phase-shift angle β at frequency $f = 140\,\mathrm{kHz}$.

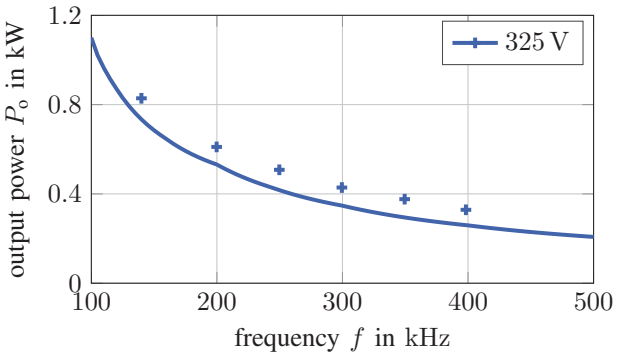

Fig. 14. Measurement (+) and simulation results (–) of output power P_o for operation of two inductors at DC-Link voltage $V_{\mathrm{dc}} = 325\,\mathrm{V}$ and varying frequency f at constant phase-shift angle $\beta = 180°$.

was built. Experimental results show, that when using two inductors, the maximum output power is 828 W, while it is 522 W when using a single inductor.

For our future work we aim to measure the system efficiency as well as making further investigations on an efficiency-optimized operation of the inverter with a focus on the presented power control schemes. Regarding the electromagnetic part of the system, we aim to improve the accuracy of the used model by inclusion of loss effects within the inductors as well as investigation of hysteresis losses within the cookware.

REFERENCES

[1] O. Lucia, P. Maussion, E. J. Dede, and J. M. Burdio, "Induction Heating Technology and Its Applications: Past Developments, Current Technology, and Future Challenges," *IEEE Transactions on Industrial Electronics*, vol. 61, no. 5, pp. 2509–2520, May 2014. [Online]. Available: http://ieeexplore.ieee.org/document/6595059/

[2] F. Rehm, P. Breining, and M. Hiller, "Determination of Electromagnetic Material Properties of Ferromagnetic Stainless Steel Used in Domestic Induction Heating Cookware," in *2022 International Conference on Electrical Machines (ICEM)*. Valencia, Spain: IEEE, Sep. 2022, pp. 1009–1014. [Online]. Available: https://ieeexplore.ieee.org/document/9910889/

[3] J. Acero, C. Carretero, I. Millán, Ó. Lucía, R. Alonso, and J. M. Burdío, "Analysis and Modeling of Planar Concentric Windings Forming Adaptable-Diameter Burners for Induction Heating Appliances," *IEEE Transactions on Power Electronics*, vol. 26, no. 5, pp. 1546–1558, May 2011. [Online]. Available: http://ieeexplore.ieee.org/document/5598533/

[4] J. Serrano, J. Acero, I. Lope, C. Carretero, and J. M. Burdio, "A Flexible Cooking Zone Composed of Partially Overlapped Inductors," *IEEE Transactions on Industrial Electronics*, vol. 65, no. 10, pp. 7762–7771, Oct. 2018. [Online]. Available: https://ieeexplore.ieee.org/document/8280509/

[5] H. Sarnago, P. Guillen, J. M. Burdio, and O. Lucia, "Multiple-Output ZVS Resonant Inverter Architecture for Flexible Induction Heating Appliances," *IEEE Access*, vol. 7, pp. 157 046–157 056, 2019. [Online]. Available: https://ieeexplore.ieee.org/document/8886573/

[6] O. Lucia, J. Acero, C. Carretero, and J. M. Burdio, "Induction Heating Appliances: Toward More Flexible Cooking Surfaces," *IEEE Industrial Electronics Magazine*, vol. 7, no. 3, pp. 35–47, Sep. 2013. [Online]. Available: http://ieeexplore.ieee.org/document/6603370/

[7] J. Acero, J. Burdio, L. Barragan, D. Navarro, R. Alonso, J. Ramon, F. Monterde, P. Hernandez, S. Llorente, and I. Garde, "Domestic Induction Appliances," *IEEE Industry Applications Magazine*, vol. 16, no. 2, pp. 39–47, Mar. 2010. [Online]. Available: http://ieeexplore.ieee.org/document/5411854/

[8] H. Sarnago, O. Lucia, A. Mediano, and J. M. Burdio, "Multi-MOSFET-Based Series Resonant Inverter for Improved Efficiency and Power Density Induction Heating Applications," *IEEE Transactions on Power Electronics*, vol. 29, no. 8, pp. 4301–4312, Aug. 2014. [Online]. Available: http://ieeexplore.ieee.org/document/6655986/

[9] P. Guillen, H. Sarnago, O. Lucia, and J. M. Burdio, "Multi-Output Resonant Power Converters for Domestic Induction Heating," in *IECON 2020 The 46th Annual Conference of the IEEE Industrial Electronics Society*. Singapore, Singapore: IEEE, Oct. 2020, pp. 4320–4327. [Online]. Available: https://ieeexplore.ieee.org/document/9254987/

[10] H. Sarnago, J. M. Burdío, and O. Lucia, "High-Frequency GaN-Based Induction Heating Versatile Module for Flexible Cooking Surfaces," in *2019 IEEE Applied Power Electronics Conference and Exposition (APEC)*, Mar. 2019, pp. 448–452, iSSN: 2470-6647.

[11] H. Sarnago, J. M. Burdío, and Ó. Lucía, "High-Performance and Cost-Effective ZCS Matrix Resonant Inverter for Total Active Surface Induction Heating Appliances," *IEEE Transactions on Power Electronics*, vol. 34, no. 1, pp. 117–125, Jan. 2019.

[12] H. Sarnago, Ó. Lucía, and J. M. Burdío, "A Comparative Evaluation of SiC Power Devices for High-Performance Domestic Induction Heating," *IEEE Transactions on Industrial Electronics*, vol. 62, no. 8, pp. 4795–4804, Aug. 2015, conference Name: IEEE Transactions on Industrial Electronics.

[13] M. Raeber, P. Amiras, and A. Heinzelmann, "Analysis on the use of non-resonant inverters in single-phase induction heating applications," in *IECON 2020 The 46th Annual Conference of the IEEE Industrial Electronics Society*. Singapore, Singapore: IEEE, Oct. 2020, pp. 4315–4319. [Online]. Available: https://ieeexplore.ieee.org/document/9254394/

[14] J. Serrano, J. Acero, I. Lope, C. Carretero, J. Burdio, and R. Alonso, "Modeling of domestic induction heating systems with non-linear saturable loads," in *2017 IEEE Applied Power Electronics Conference and Exposition (APEC)*. Tampa, FL, USA: IEEE, Mar. 2017, pp. 3127–3133. [Online]. Available: http://ieeexplore.ieee.org/document/7931144/

[15] F. Rehm, P. Breining, and M. Hiller, "A measurement method for the characterization of the ferromagnetic bottom layer of cookware used in domestic induction heating," in *IECON 2021 47th Annual Conference of the IEEE Industrial Electronics Society*. Toronto, ON, Canada: IEEE, Oct. 2021, pp. 1–6. [Online]. Available: https://ieeexplore.ieee.org/document/9589834/

[16] O. Lucía, J. M. Burdío, I. Millán, J. Acero, and L. A. Barragán, "Efficiency-Oriented Design of ZVS Half-Bridge Series Resonant Inverter With Variable Frequency Duty Cycle Control," *IEEE Transactions on Power Electronics*, vol. 25, no. 7, pp. 1671–1674, Jul. 2010. [Online]. Available: http://ieeexplore.ieee.org/document/5409683/

[17] C. Carretero, R. Alonso, J. Acero, and J. M. Burdio, "Optimized 4-coil inductor system arrangement for induction heating appliances," in *IECON 2015 - 41st Annual Conference of the IEEE Industrial Electronics Society*. Yokohama: IEEE, Nov. 2015, pp. 004 948–004 952. [Online]. Available: http://ieeexplore.ieee.org/document/7392876/